



HAL
open science

3D cellular automata simulations of intra and intergranular corrosion

Dung Di Caprio, Janusz Stafiej, Giorgio Luciano, Laurent Arurault

► **To cite this version:**

Dung Di Caprio, Janusz Stafiej, Giorgio Luciano, Laurent Arurault. 3D cellular automata simulations of intra and intergranular corrosion. *Corrosion Science*, 2016, 112, pp.438-450. 10.1016/j.corsci.2016.07.028 . hal-02049434

HAL Id: hal-02049434

<https://hal.science/hal-02049434v1>

Submitted on 26 Feb 2019

HAL is a multi-disciplinary open access archive for the deposit and dissemination of scientific research documents, whether they are published or not. The documents may come from teaching and research institutions in France or abroad, or from public or private research centers.

L'archive ouverte pluridisciplinaire **HAL**, est destinée au dépôt et à la diffusion de documents scientifiques de niveau recherche, publiés ou non, émanant des établissements d'enseignement et de recherche français ou étrangers, des laboratoires publics ou privés.




Open Archive Toulouse Archive Ouverte (OATAO)

OATAO is an open access repository that collects the work of Toulouse researchers and makes it freely available over the web where possible

This is an author's version published in: <http://oatao.univ-toulouse.fr/21895>

Official URL: <https://doi.org/10.1016/j.corsci.2016.07.028>

To cite this version:

Di Caprio, Dung and Stafiej, Janusz and Luciano, Giorgio and Arurault, Laurent  *3D cellular automata simulations of intra and intergranular corrosion*. (2016) *Corrosion Science*, 112. 438-450. ISSN 0010-938X

Any correspondence concerning this service should be sent to the repository administrator: tech-oatao@listes-diff.inp-toulouse.fr

3D cellular automata simulations of intra and intergranular corrosion

D. di Caprio^{a,*}, J. Stafiej^b, G. Luciano^{c,d}, L. Arurault^e

^a *Chimie ParisTech, PSL Research University, CNRS, Institut de Recherche de Chimie Paris (IRCP), F-75005 Paris, France*

^b *Cardinal Stefan Wyszyński University, Department of Mathematics and Natural Sciences, Wóycickiego 1/3, Warsaw, Poland*

^c *Institute of Marine Science – National Research Council, ISMAR-CNR, Via De Marini, 6 – IV P., 16149 GE, Italy*

^d *Institute for the Study of Macromolecules – National Research Council, ISMAR-CNR, Via De Marini, 6 – IV P., 16149 GE, Italy*

^e *Cirimat, Université de Toulouse, UPS/INPT/CNRS, 118 route de Narbonne, 31062 Toulouse Cedex 9, France*

ARTICLE INFO

Keywords:

Intergranular
corrosion Modelling
Cellular automata
Exfoliation corrosion

ABSTRACT

A simple model for the effect of intergranular corrosion on overall corrosion processes is investigated using a cellular automata approach. The corroding polycrystalline material consists of domains and their boundaries. The domains represent the monocrystalline cores while their boundaries represent the intergranular defects. Either, a periodic pattern or randomly generated domains of Voronoi tessellation are used to represent the polycrystalline structure. The parameters of the model, taking into account the polycrystalline aspect of corrosion, are the domain density and the corrosion probabilities of metal grain core and grain boundary sites. The corrosion probability for grain boundary is set to a value higher than it is for the grain core. A complex surface structure appears with a high geometrical roughness when defects are not too dense. A strong correlation is established between the roughness evolution, the metal crystalline properties and the corrosion mechanism of metal dissolution. This work concerns simulations in 3D and extends the previous work limited to 2D simulations.

1. Introduction

Physical properties of materials e.g. mechanical properties are strongly dependent on structural features, such as grain sizes of the polycrystalline material [1]. This is also true for susceptibility/resistivity to corrosion. It is known, for instance, that susceptibility to corrosion increases with the roughness [2,3] related with the presence of intergranular material and granular junctions at the outer surface of the material.

A common type of corrosion attack, for which the grain structure is important, is intergranular (IGC) or intercrystalline corrosion. IGC is defined [4] as a selective corrosion of grain boundaries or closely adjacent regions without considerable attack on the grains or crystals themselves. In IGC, the grain boundaries become anodic and the bulk material between the grain boundaries is not affected and therefore becomes cathodic. Due to its nature, IGC penetrates more quickly than pitting corrosion and it has drastic effect as a stress riser, in comparison to pitting corrosion, reducing the number of cycles required to initiate a fatigue crack [5]. The same kind of subsurface fissure can be produced by transgranular corrosion

where a small volume of metal is removed in preferential paths that proceed across or through the grains. Alloys with enhanced resistance to corrosion as well as methodologies to analyze, predict corrosion development and avoid corrosion failures remain a very active field of research. This is confirmed by a selection of recent articles found on the topic [6–18].

Cellular automaton models (CA) based on discretized description of time, space and states, have been applied successfully for modelling pitting corrosion and passivation/depassivation events [19–31]. The present study is an extension in 3D of a previous 2D numerical model [32–36] simulating the effect of the grain size on the corrosion processes by using a CA model focusing on intra and intergranular corrosion (IGC). It adds to recent findings published in this field [37].

In this work, both surface properties and internal bulk structure of the material are investigated. The focus of this paper is on geometrical effects of the grain shape and their spatial organization in the system. The objective is to study how fast corrosion can penetrate into material and besides chemical dissolution of the corroded material determine the effect of pure mechanical detachment of chunks of material. These chunks are nearly always partially dissolved grains of polycrystalline material when their link to the bulk material becomes corroded by the faster intergranular corrosion. The chunk effect may also occur in random dissolution

* Corresponding author.

of the material when the external medium grows as in the Eden model [38]. Originally, the medium is defined a connected set. However, the material may form peninsulas detached as islands when a straight corrosion cuts the peninsula from the mainland. This chunk effect gives a plausible explanation for non-faradaic material loss in some electrode processes. The inhomogeneous granular structure leads to an enhancement of this scenario [32]. The modelling is very simple. The grain cores are embedded in intergranular material. Both the core and intergranular materials are homogeneous and isotropic. Cores are more resistant to corrosion therefore the corrosion proceeds by dissolving intergranular material at grain boundaries. Ultimately, grain cores “fall off” when the intergranular material around them gets corroded. The progression of the corrosion front is to some degree delayed, compared to “pure intergranular material”, by the sinuosity effect of the lines of “steepest descent” from the surface. These lines can be described as the “shortest path” within the intragranular space connecting two points on a line normal to the surface. There is a sinuosity coefficient due to the fact that the line cannot go through the cores. Imagine a signal is sent from one of the points to another propagating isotropically and with constant speed. Compare the time of arrival in two cases. In the first event, the signal is allowed to propagate only in intergranular space and in the second case it propagates in both cores and intergranular spaces ignoring the difference. The ratio between the two lengths of time is the sinuosity coefficient. In our model, the sinuosity coefficient is the main consequence of the granular structure of the material. It is isotropic for the Voronoï tessellation but, in general, it is direction dependent.

2. Model

As in [32], let us consider a simplified model of intergranular corrosion. The grain boundaries are assumed to be the only defect of the crystalline structure susceptible to enhance corrosion rate. The intergranular region has chemical and physical properties distinct from that of the grains. A common occurrence is segregation or depletion of some components of the alloys in the intergranular region [39–47]. For instance, in the case of sensitized stainless steels, chromium carbide precipitates fragilize the intergranular region [48]. In general, several different components can segregate at the grain interface, such as phosphorous, tin, silicium, nickel, leading by different mechanisms to a higher susceptibility to corrosion of the material [49,50]. In this paper, the focus is on the difference in corrosion kinetics between intra and intergranular corrosion. Consequently, the dependence of corrosion on crystalline orientation is not taken into account. The grains of polycrystalline material are presented as homogeneous isotropic domains arranged as adjacent polyhedra in three dimensional space. The material, in the thin intergranular spaces of the polygonal faces of the polyhedra, is regarded as more susceptible to corrosion than the grain cores.

Let us look at regular structured fillings of three dimensional space analogous to those shown in [32] in two dimensions. The first case, referred to as *cube piling* (CP), is a regular piling with cubes one above the other with matching edges. The second case, referred to as *brick piling* (BP), is a regular piling, with the edges of the cubes shifted by half a lattice dimension in the two directions parallel to the metal surface with respect to the plane below. Finally, three dimensional Voronoï tessellation is considered as an example of non periodic irregular structures.

The Voronoï tessellation is obtained by randomly generating a number of vertices with uniform distribution corresponding to a given density or, conversely, to the average domain volume. Periodic boundary conditions in all directions are used for the vertices to avoid deformation of the Voronoï tessellation at the facets of the

simulation cube. The domains start growth at the vertices. Initially they form vertex centred spheres. Gradually, the domains grow by slightly incrementing the radius and including points which do not belong to another sphere. The growing domains meet ultimately at the faces of Voronoï polyhedra if growth starts simultaneously and growth rate is identical at all vertices. The two nearest neighbouring sites, each belonging to different domains, are marked as intergranular sites in our lattice version of the growth process.

It is possible to represent this system on a discrete, three dimensional lattice, $N_x \times N_y \times N_z$ where N_i , $i = x, y, z$ are the integer dimensions of the lattice in the three directions. In our model, there are three types of lattice sites corresponding to the inter, the intra-granular material and the solution. The solution corresponds to an aggressive, corrosive environment – acidic solution for instance. The top z plane is composed of solution sites and below lies the bare metal made of granular and intergranular material. Hence, the direction z is the direction perpendicular to the metal surface, which also corresponds to the main direction in the propagation of corrosion. Periodic boundary conditions are used in the plane parallel to the x and y directions. The cellular automata lattice approach adopts a mesoscopic viewpoint. As in [51,52], to relate the simulation to the real world, space and time equivalence for our pixel size and simulation time step must be set in terms of real dimensions. In this paper, a cube of lateral dimension $a = 0.2 \mu\text{m}$ is chosen for the pixel size, a size sufficiently small for a typical grain dimension as chosen in this paper [53,54]. The time scale is set considering a corrosion process for the intergranular material of 1 mm/y . With the above value of a , the simulation time step corresponds to of 6310 s . Such value is comparable to that illustrated in [17]. In this paper, the authors find that in one instance a period of 1000 h corresponds to the detachment of one layer of grains of characteristic dimension $84 \mu\text{m}$. In one year, the corrosion rate corresponds approximately to 0.74 mm/y . The round value of 1 mm/y adopted here is consistent with the above experimental value, and simplifies discussion for the case studies discussed in this paper.

The intergranular region has a width of two lattice sites. This value is a minimal value chosen in order to ensure a regular propagation of corrosion in the intergranular region. The characteristic dimensions of the intragranular domains will be specified in more detail later, as grains may not be isotropic. Typically, they are between 6 and $24 \mu\text{m}$, which is in the range of a micrometre to $100 \mu\text{m}$ found in the literature [53,54], although smaller than the grains studied in [17]. Clearly, the order of magnitude is only indicative, as real systems may have grains of different dimensions depending on the metallurgical treatment or the “history of the sample”. The corrosion rates of inter and intragranular material depend on the treatment and also on aggressiveness (temperature, pressure, composition) of the external environment in contact with the metal.

In our simulation, the active sites susceptible to corrosion are those which have a neighbouring solution site. It means that during a time step they are converted to the solution site with a certain probability. The intergranular material can corrode with a probability p_{ig} which can be set to $p_{ig} = 1$. Choosing a different value rescales the correspondence between the simulation time step and the real corrosion rate. The choice is arbitrary in the sense there are many possible sets of values of simulation time step and p_{ig} corresponding to the same corrosion rate. This means that $p_{ig} = 1$ and time step of 6310 s can also be simulated by $p_{ig} = 0.5$ a time step of 3155 s . In terms of computational efficiency $p_{ig} = 1$ is the better choice, as each computational time step results in an intergranular corrosion, whereas the second choice would require double the number of simulation steps. In both cases the physical corrosion rate is identical.

The grain material can corrode with a probability p_g . With the choice of $p_{ig} = 1$, the corrosion rate for the grain is seen as

relative to the corrosion rate of the grain boundaries and $p_g < 1$ is assumed.

At each time step, the lattice sites in contact with the aggressive environment dissolve according to the probabilities p_{ig} and p_g . Furthermore, any metal material disconnected from the main piece is removed. By convention, the main piece is connected to the lowest bottom part of the metal. Corrosion proceeds downwards and the connectivity check starts from the bottom up to the top surface. The top surface is exposed to solution and susceptible to corrosion.

The average height at a time step t is given as:

$$\bar{h}(t) = \frac{1}{N_x N_y} \sum_{x,y=0}^{N_x, N_y} h_{x,y}(t) \quad (1)$$

where $h_{x,y}(t)$ is the height (z-coordinate) of the topmost site of the material column over the site referenced by x and y in the xy plane. The mean squared deviation of $h_{x,y}(t)$ averaged over the (x, y) surface is denoted $\bar{\sigma}(t)$

$$\bar{\sigma}(t) = \left[\frac{1}{N_x N_y} \sum_{x,y=0}^{N_x, N_y} (h_{x,y}(t) - \bar{h}(t))^2 \right]^{1/2} \quad (2)$$

and it serves as a measure for surface roughness.

3. Results

3.1. Model grains: cube and brick pilings

In the following, results of simulations performed with grain size of 64 lattice units for the cube and brick pilings are presented. The simulation box size is $512 \times 512 \times 4096$ sites. It is 512×512 in lateral size (horizontal plane) and 4096 sites high. The simulation

stops when corrosion reaches the plane next to the bottom (one above the bottommost layer of sites). Hence, the simulation time with $p_{ig}=1$ is of the order of 4000 time steps corresponding to approximately 7000 h i.e. 290 days at the chosen corrosion rate for intergranular material of 1 mm/y.

3.1.1. Intergranular corrosion, $p_g=0$ for CP

3.1.1.1. Height and roughness. First, consider the corrosion of the intergranular region, leaving intact the grain cores $p_g=0$. The average height as a function of time is shown in Fig. 1.

The curves show that the average height follows a step like behaviour. They remain almost constant and drop abruptly when the layer of cubes detaches. The linear regression lines for both models are quasi identical, the expression is $h_{lr}(t) = 4141 - 0.9994t$, the slope is around -1 in both cases. This is in contrast to what has been shown for the two dimensional systems and will be discussed further on. In this specific case, the effective corrosion rate of the sample remains 1 mm/y, i.e. the nominal corrosion rate of the intergranular material multiplied by the coefficient in front of t which is almost 1.

Fig. 2 shows the roughness of the surface plotted as a function of time. The regular oscillations of roughness correspond to the corrosion and detachment of an entire layer of grains. The mechanism is detailed later on. Before detachment the roughness increases gradually to drop sharply at the time of detachment of a layer of grains. Due to symmetry of the system, in the absence of intragranular corrosion, detachment takes place simultaneously for all grains across the metal surface. Once all the grains in a layer detach, the layer becomes smooth again and the roughness is at its minimum. The roughness oscillations are similar for both CP and BP geometries although they do not have exactly the same magnitude. The maximum roughness for BP geometry is lower

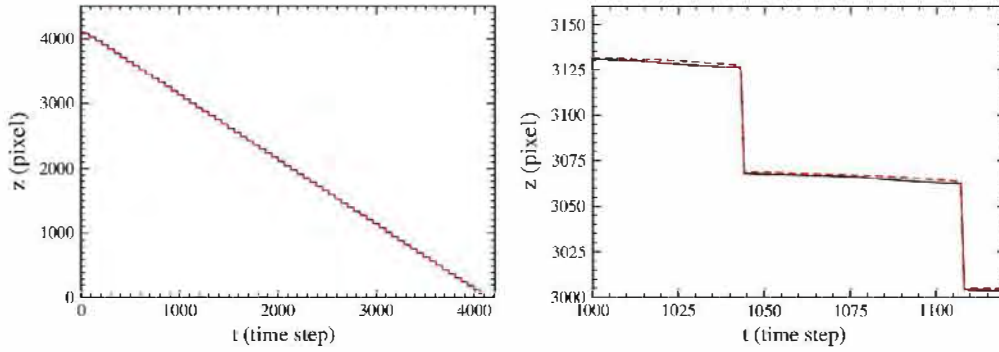


Fig. 1. Corrosion height as a function of time and on the right a detail of the plot. Full black line is for the cube piling and red dashed line for the brick piling. (For interpretation of the references to colour in this figure legend, the reader is referred to the web version of the article.)

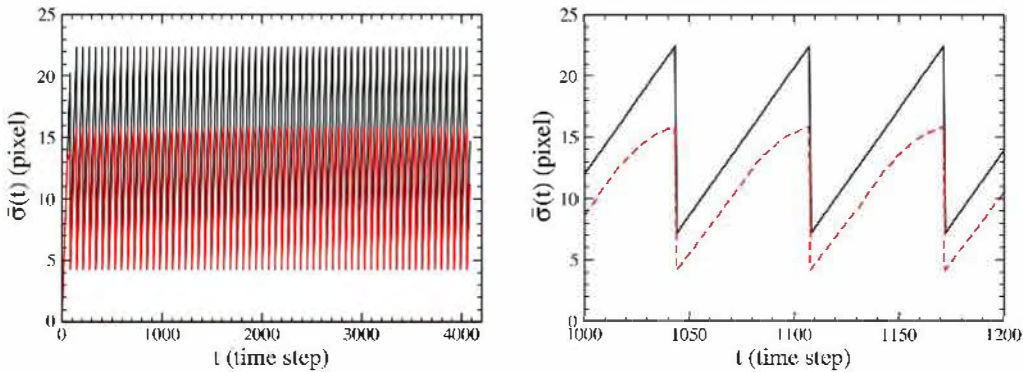


Fig. 2. Surface roughness as a function of time and on the right a detail of the plot. Full black line is for the cube piling and red dashed line for the brick piling. (For interpretation of the references to colour in this figure legend, the reader is referred to the web version of the article.)

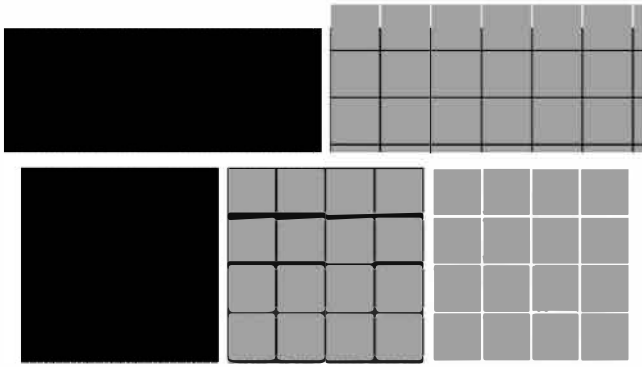


Fig. 3. Vertical and horizontal sections of the corroded metal with the intergranular region in black and the metal grains in grey. The grains have 64 lattice sites dimensions. First, at the top, the vertical sections are taken across the intergranular region and outside of it. Below, the horizontal planes correspond to a section across the intergranular region, and sections 16 and 48 planes above it.

than the roughness for CP geometry, while the BP minimum is higher than the CP minimum.

3.1.1.2. System cross sections. To better understand the differences between the two geometries, we show horizontal and vertical cross sections of the material at different time steps – characteristic of grain detachment. The vertical cross sections are chosen for planes spaced less than half the grain size, as there are symmetries across half of the grain in the x and y directions.

First, the CP in a configuration three time steps after detachment is described. The characteristic sections are shown in Fig. 3. The intergranular material fills the horizontal and vertical planar

slits between the cubes up to the horizontal level reached by corrosion. As a consequence, the horizontal sections above and below differ in that above the corrosion level the vertical slits are filled with solution and below the corrosion level they are filled with intergranular material. Another scenario occurs in the horizontal slit above the corrosion level just before the detachment. Some of the intergranular material remains in the slit and keeps the top cubes attached to the rest of the corroded piece. This is illustrated in Fig. 4 corresponding to three time steps before detachment. The cross sections show that once the corrosion level attains the horizontal slit, the corrosion can proceed horizontally inwards from the edges to the centre of the facets. The top level grains remain “glued” to the system by contacts until they undergo corrosion and the layer of grains detaches. This horizontal corrosion phase takes time and, just after grain detachment, the corrosion is already well below the new material surface – as seen in Fig. 3.

3.1.2. Intergranular corrosion, $p_g = 0$ for BP

The phenomenon is quite different in the BP structure despite the quasi identical evolution in corrosion (Fig. 1).

In Fig. 5, planar cross sections are shown at three time steps after detachment of a layer of cubes, i.e. just after the rugosity minimum. Fig. 5 shows that at this time step corrosion proceeds downwards, mostly from the top layer of cubes, along the slits between the cubes. The combined horizontal and vertical corrosion leads to the sawtooth pattern visible in the figures.

In Fig. 6, the sections correspond to three time steps before detachment of the grains, when maximum roughness is reached. Just before grain detachment, the sawtooth pattern is also present in the regions between grains but now in the top horizontal intergranular planes there is a diagonal mesh-like structure.

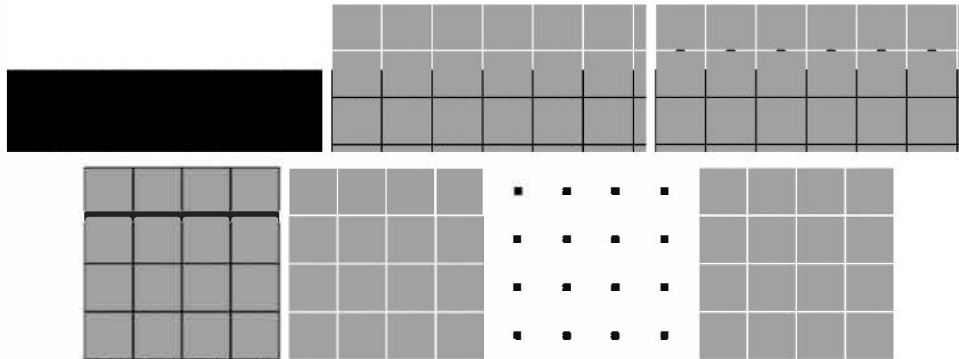


Fig. 4. Vertical and horizontal cross sections of the corroded metal. At the top, the vertical planes correspond to planes in the vertical intergranular region between grains, on quarter of the grain size and in the middle of the grain. At the bottom, the horizontal planes are for planes situated half and a quarter grain size below the intergranular horizontal plane between cube layers. Then, across this plane and half the grain size above it.

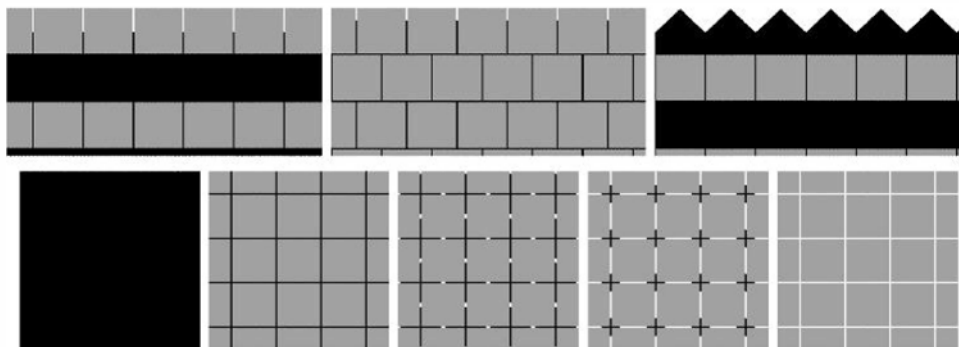


Fig. 5. Vertical and horizontal cross sections of the corroded metal. The first vertical section correspond to a section across the vertical intergranular region of the middle layer of grains in the image then planes one quarter and half a grain size from this plane. The horizontal sections are for the top intergranular dividing plane. Then, for planes a quarter, half, three quarters and an approximately one grain size above this plane just above the sawtooth top.

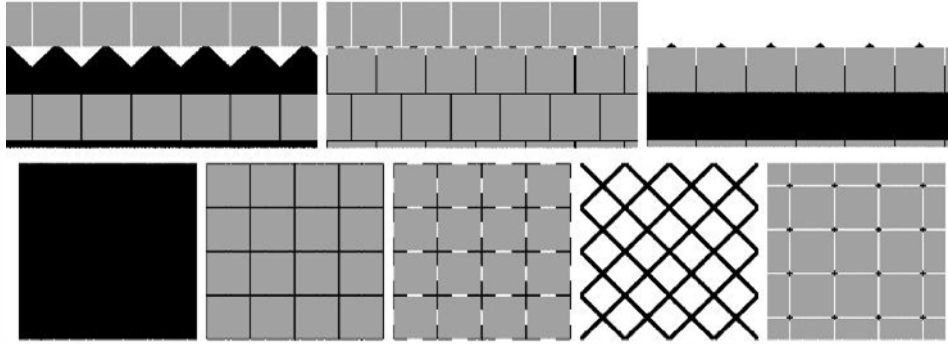


Fig. 6. Vertical and horizontal cross sections of the corroded metal. The first vertical section correspond to a section across the vertical intergranular region of the middle layer of grains in the image then planes one quarter and half a grain size from this plane. The horizontal sections are for one before the top intergranular dividing plane. Then, for planes half, three quarters, one grain size above this plane and finally just across the sawtooth top.

This structure results from the horizontal corrosion as previously described. However, the horizontal corrosion proceeds from the middle of the edges outwards. This location is the junction with the middle of the edges of the cubes above which are oriented perpendicularly. Conversely, for CP, the corrosion proceeds from the edges towards the middle of the facet. The intergranular material patterns, in the horizontal plane, slightly below the top layer of cubes, are distinctly different for the CP and BP geometries just before detachment. There are small spots of contact in the case of CP piling, while there is a mesh formation in the case of BP. This phenomenon could have a bearing on the tendency to detachment of the grains, for instance, in the case of exfoliation.

Finally, the left and right vertical sections in Figs. 5 and 6 show that there is a thin vertical line of intergranular material common to two successive layers of grains. Therefore in contrast to the two dimensional case, the corrosion can proceed vertically along this line, and no consecutive horizontal and vertical corrosion sequence is necessary. As a result, the same average corrosion rates and the slope -1 for corrosion advancement curves $h(t)$ characterize both CP and BP cases.

3.2. Metal grains of the Voronoï tessellation form

Based on an experimental structure, Fig. 7, Voronoï tessellation is now considered as a more realistic model for grains of



Fig. 7. Optical microscopic 3D views of the AA 7175T7351 substrate after degreasing and metallographic attack [55].

polycrystalline material. An example of the initial system geometry (IVT) is shown in Fig. 8. From Voronoï tessellation an alternative case can be easily obtained corresponding to the rolled treatment of metals. To be specific, consider grains elongated by a factor 4 in one direction (L) and contracted by an equal factor 4 in one of the perpendicular directions, the short transverse direction (ST). The remaining direction, the long transverse direction (LT), is left unchanged. The elongation and contraction having the same ratio, the overall average volume of the grains is left unchanged compared to the reference IVT case. Now the material is inhomogeneous. Corrosion rates depend on the direction, and take the form of a symmetric tensor where the elongation, contraction and remaining direction are the tensor normal axes.

The height as a function of time is shown in Fig. 9.

The linear regression for the IVT is $h_{lr}(t) = 4151 - 0.8090t$. Here, the effective corrosion rate of the material is 0.809 mm/y. The slope is lower than the slope for the CP, BP geometries. These are more “efficient”, in both geometries there are vertical straight paths which optimize the vertical corrosion process. In [32], the angle of the slope is also used as an added measure of corrosion obliqueness. The slope is a tangent to this angle. The corrosion is faster than it is for the brick and Voronoï geometries in two dimensions with a slope of 2/3. This is likely as the brick geometry has a slope 1 and Voronoï should be situated below this limit. The IVT geometry corresponds to a progression angle $\theta = 37.8^\circ$ degrees with respect to the vertical for the equivalent system with regular linear oblique corrosion.

When the corrosion is parallel to the elongation direction (L), the linear fit is $h_{lr}(t) = 4166 - 0.9357t$. Here, the corresponding angle is $\theta = 21.4^\circ$ degrees with respect to the vertical. The effective corrosion rate of the material is now 0.9357 mm/y.

The case where the corrosion is parallel to the invariant (LT) axis, the linear fit is $h_{lr}(t) = 4160 - 0.9260t$. The corresponding angle is $\theta = 22.5^\circ$ degrees with respect to the vertical. The effective corrosion rate of the material is then 0.9260 mm/y.

And finally, when the corrosion is parallel to the transversal axis with contraction (ST), the linear fit is $h_{lr}(t) = 4130 - 0.5193t$. The corresponding angle is $\theta = 58.7^\circ$ degrees with respect to the vertical and the corrosion is much slower than in all other cases. The effective corrosion rate of the material is 0.5193 mm/y.

We draw attention to the fact that the fastest and slowest corrosion rates – respectively the directions of corrosion parallel to (L) and (ST) axes – differ by a factor of approximately 1.8, a significant value.

The roughness is shown in Fig. 10.

Obviously, the variations in roughness are no longer periodic as they are in the CP and BP structures.

Finally, Fig. 11 illustrates images of the system corroded in the (L), (LT) and (ST) directions.

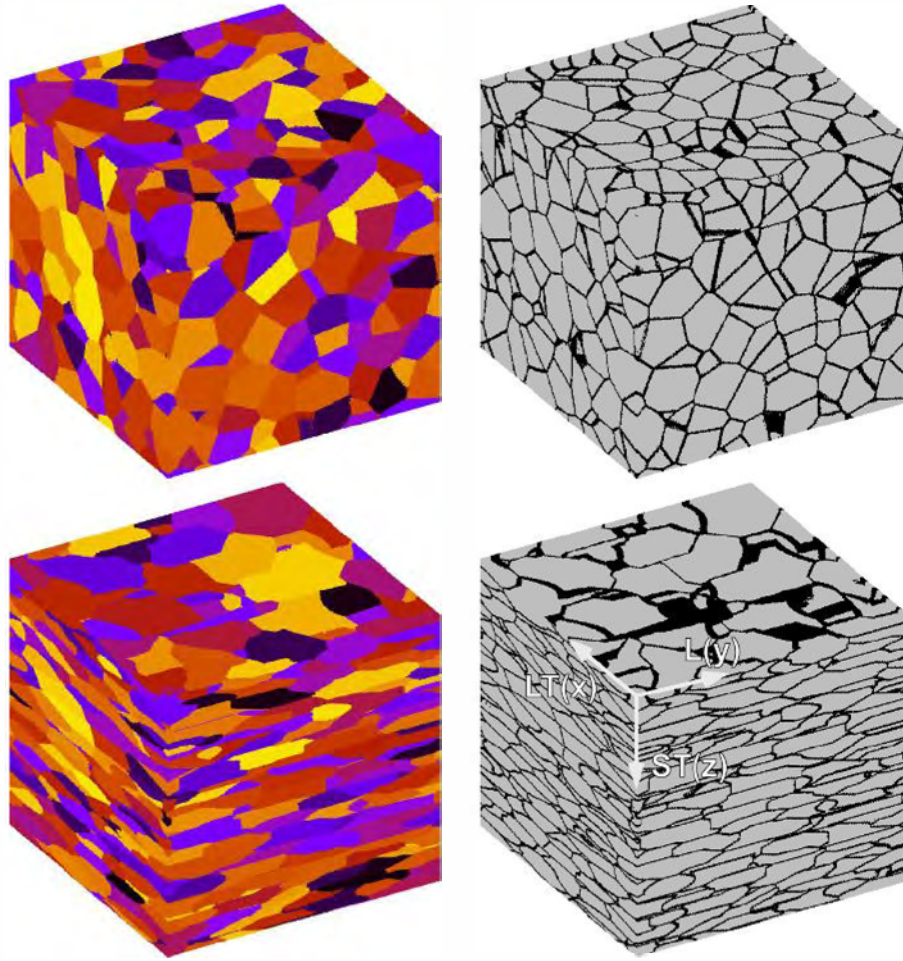


Fig. 8. Granular material with an isotropic Voronoi tessellation (IVT) (top) and granular material from rolled treatment (bottom) where the elongation (L) is in the direction y, long transversal (LT) is in direction x and short transversal (ST) in direction z. The elongation and contraction factor for (L) and (ST) is 4 while for (LT) it is unchanged compared to the IVT. First each grain is marked with a distinct colour. Then only the intra and inter-granular materials are marked.

Note that corrosion rates in the directions (L) and (LT) have the same magnitude and show a corrosion rate faster than in the IVT. Conversely, corrosion in the (ST) direction is considerably slower and even slower than in the case of IVT. These tendencies can be explained if one bears in mind that the intergranular corrosion applies to phases where the corrosion evolves horizontally. The corrosion in the directions (L) and (LT) share the (ST) direction

in the horizontal plane, which is related to a fast horizontal corrosion process. On the other hand, corrosion in the (ST) direction involves slow horizontal corrosion processes along the (L) and (LT) directions. The roughness follows the same trend with comparable magnitude of roughness for the (L) and (LT) corrosion directions. Roughness is slightly larger for (L) direction due to larger expansion rate in the corrosion direction. Smaller roughness is found for the IVT and even smaller for the (ST).

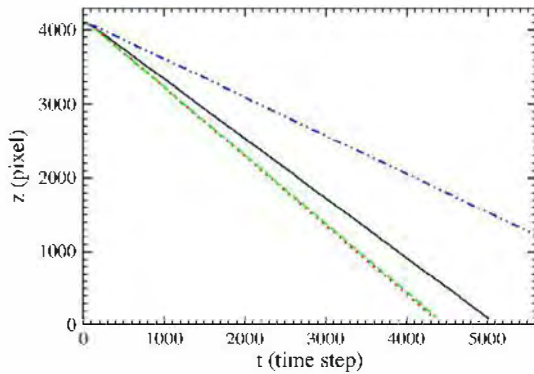


Fig. 9. Corrosion height as a function of time for the IVT (black line) and with elongation/contraction in the z/x (red dotted line), with elongation/contraction in the y/x (green dashed line), with elongation/contraction in the y/z (blue dot-dot-dashed line). (For interpretation of the references to colour in this figure legend, the reader is referred to the web version of the article.)

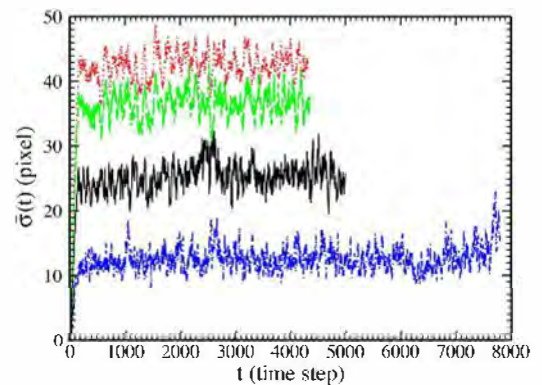


Fig. 10. Roughness as a function of time t for the geometries used in Fig. 9 and with identical colour codes for the lines. Full lines are used because the curves are quite rough.

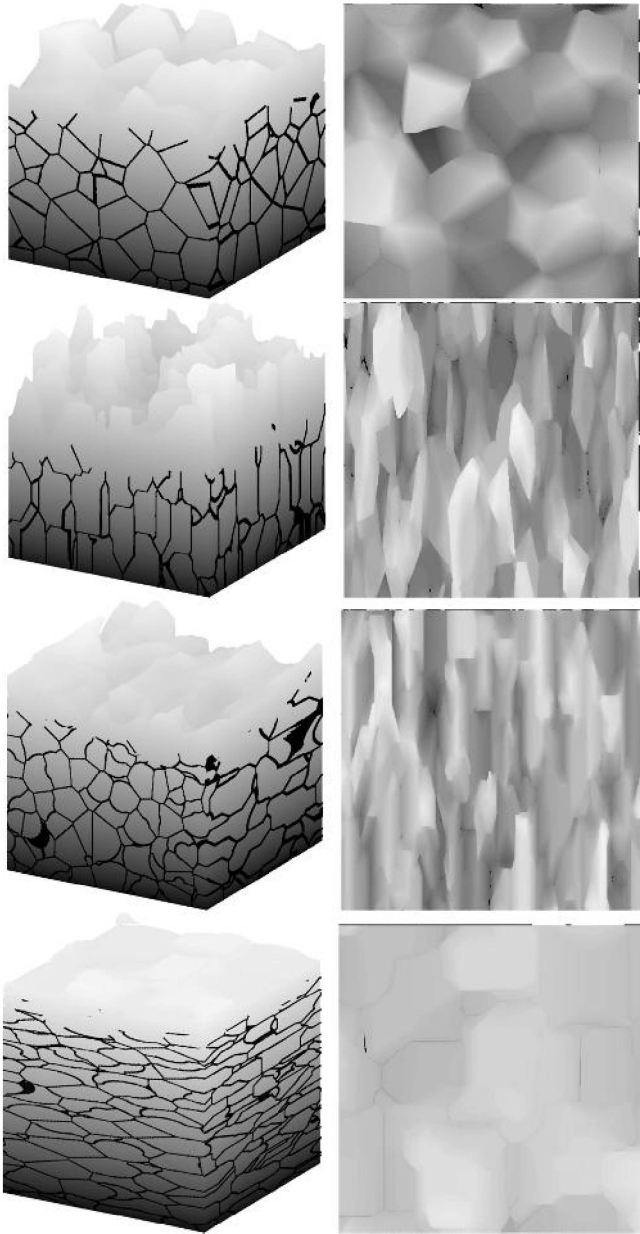


Fig. 11. Side and top views of the corroded system with IVT, with elongated grains and with (L), (LT) and (ST) respectively directed along the following axis: $z, y, x; y, z, x$ and finally y, x, z . The direction of the axis is the one given in Fig. 8.

For rolled material the grains are elongated and oriented in the rolling direction if no further thermal treatment is applied.

The slowing down of corrosion in the (ST) case can be comprehended when we think of the brick geometry in two dimensions [32], characterized by a slower corrosion rate than the square structure. In the brick structure, the system is forced into regimes of horizontal corrosion in order to successively find ways for the vertical corrosion. The same occurs in three dimensions when the layers of “plaquettes” are organized parallel to the metal surface. Note that here plaquettes are more difficult to remove, and this for instance has repercussions on the kinetics of exfoliation.

For corrosion progress along (L) and (LT) directions of the grains, the corrosion rate is larger compared to IVT, as the steepest descent lines on the grain boundaries are longer than for IVT by a coefficient equal to the elongation factor. The difference between corrosion along the (L) and (LT) directions appears to be relatively small.

Scantly faster corrosion and higher roughness occur when corrosion propagates in the (L) direction of the largest elongation.

The above results characterize corrosion for different material structures and surface orientation in steady state conditions. The initial evolution can be described by considering examples of the surface morphologies at the initial stages of the corrosion process. Let us take the IVT case at two different stages in time. First, when corrosion has progressed on a length scale smaller than the average grain size – 64 lattice sites in our simulations. Second, when the corrosion progress is larger than the average grain size.

Fig. 12 shows the initial stages when grains start “falling out” from the initial flat surface. The images indicate that the corroded spots where the grains have “fallen out” are not uniformly distributed. There are clusters of grains forming flat areas at the surface, with practically no grain detachment, and rough regions with detached surface grains. At the top surface, the initial distribution of grain sizes which results from the section of 3D tessellation with a plane, can differ from the distribution of grains sizes in the volume. The surface grains are more or less strongly embedded into the substrate below. However, the initial detachment of a grain seems to facilitate the detachment of the neighbouring grains, leading to correlation between corroded and noncorroded surface areas. The simulated surface resembles the experimental image of intergranular corrosion shown in Fig. 13.

3.3. Intergranular and intragranular corrosion

In this section, the combined effect of intergranular and intragranular corrosion is considered. The intragranular corrosion rate value is $p_g = 0.25$. This value corresponds to a corrosion rate smaller than for intergranular corrosion, yet of the same order of magnitude.

3.3.1. Cube piling

For the simple CP, two typical side views are given in Fig. 14, corresponding to a few time steps before and after detachment of a plane of grains.

The side views before detachment, in Fig. 15, show the peculiar shape of the grains just before detaching.

The typical V-shape corrosion groove is formed. It is characteristic of the combined effects of faster intergranular corrosion (bottom pointed “V” shape) and the “V” shape opening due to intragranular corrosion [17,56,57]. Peninsulas form as a combined effect of intra and intergranular corrosion. The last image of Fig. 15 resembles the scheme of Fig. 16 obtained by combining the main V-shape vertical corrosion groove with the V-shape horizontal corrosion groove.

The side views after detachment in Fig. 17 show grains at the beginning of their corrosion. The grains have the predictable shape of cubes eroded from the top edges downwards leading to the V reentrant shape.

These shapes resemble those illustrated in the 2D model in [17].

3.3.2. Brick piling

For the BP geometry, two typical side views are given in Fig. 18 corresponding to a few time steps before and after detachment of a plane of grains. The sections before detachment, in Fig. 19, show the peculiar shape of the grains before detachment, resembling cones with cross shaped sections. The sections after detachment are shown in Fig. 20. They have a shape similar to that of CP, but combined with emergence of a cross shaped section at the top. For the BP, we find that the possible shapes of the grains visible in Figs. 18 and 19 just before detachment might in 3D have a larger variety than could be foreseen by extrapolating the 2D model in [17]. In particular, they need not have convex geometries.

The overall corrosion rates for CP and BP geometries are not shown as they are similar to those in the absence of intragranular

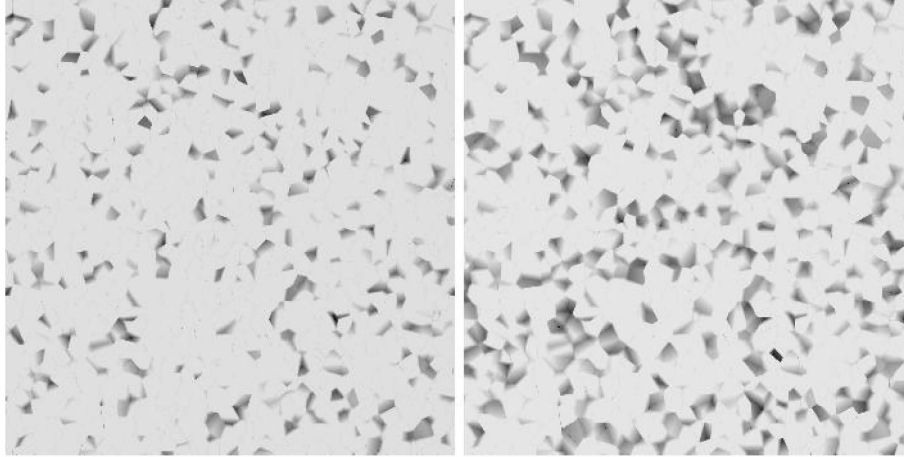


Fig. 12. Initial top view of the layer after 55 and 70 corrosion steps. Here larger planes of lateral dimension of 2048×2048 are shown.

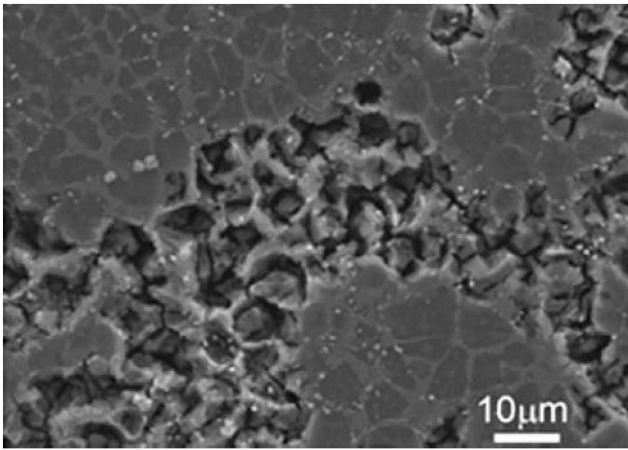


Fig. 13. SEM micrographs of polished AE44 coupons during immersion test subject to intergranular corrosion. Reprinted from Ref. [2].

corrosion – the slope is of the order of -1 . As long as intragranular corrosion is slower than intergranular corrosion, the overall corrosion process is dominated by the grain detachment whose kinetics remains identical. The ratio of intra to intergranular corrosion affects mainly the shape of the grains that “fall out” as well as the roughness shown in Fig. 21. The more complex grain shape, for the BP, results from the shifted grain junctions in the vertical planes for successive layers. The roughness is lower than it is in the absence of intragranular corrosion, because the top grains end up smaller as a result of the intragranular corrosion. Again, the roughness appears higher in BP geometry than in CP geometry.

Note that the intergranular rate p_g can be related to the groove angle α introduced in [17,56,57]. Here the ratio of the intergranular corrosion rate to the intragranular corrosion rate is the ratio between the respective probabilities. This translates into the relation

$$\frac{1}{\sin(\alpha/2)} = \frac{p_{ig}}{p_g} \quad (3)$$

In our case, $p_{ig} = 1$ and we have the simple relation

$$\sin(\alpha/2) = p_g \quad (4)$$

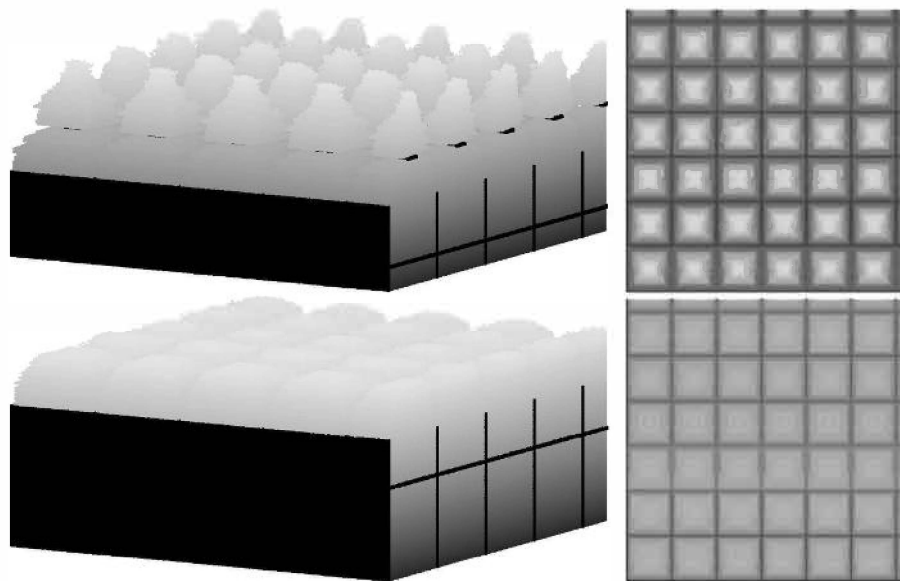


Fig. 14. Initial side and top views of the CP at two characteristic times before detachment and after detachment in presence of intragranular corrosion.

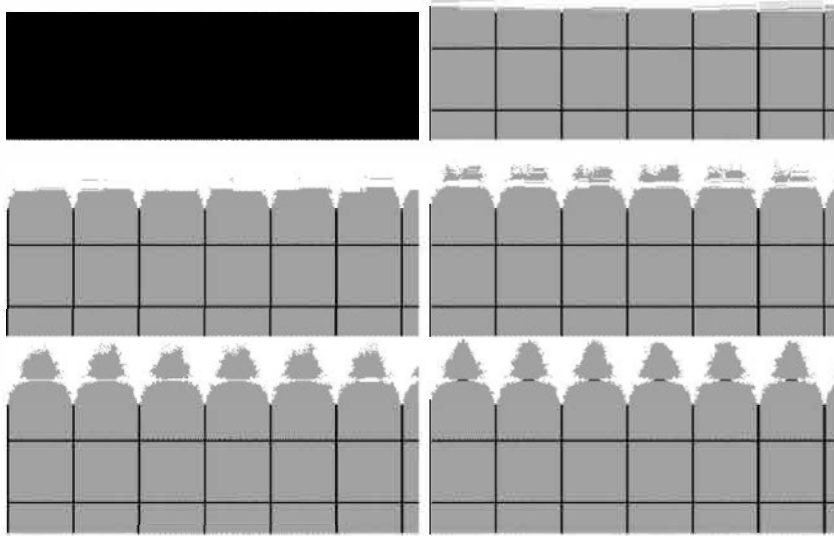


Fig. 15. Sections of the CP before detachment of the grains. To the exception of the first two images which show the intergranular plane and the next plane, all other planes are spaced of 8 planes, which corresponds to an eighth of the grain size. The planes beyond the 32nd plane are not shown as they are symmetric with respect to the middle of the elementary cube.

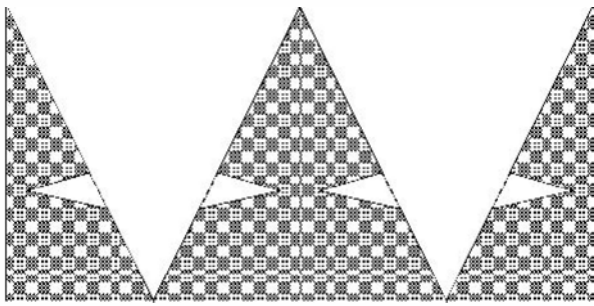


Fig. 16. Pattern obtained from a combined inter and intragranular corrosion in two competing directions vertical and horizontal.

In [17], the experimental values of the angles were distributed between 5° and 15° , which can be roughly averaged at 10° . This would approximately correspond, in the present model, to $p_g = 0.087$. As for [57], the angle is close to 25° corresponding to $p_g = 0.22$. Here, for numerical applications, the larger value of $p_g = 0.25$ has been taken to evidence the effects of intragranular corrosion. The angle of approximately 29° corresponds to the angles

observed at the tip of the grooves, in contact with the grain boundaries, as seen in Figs. 15, 17, 19, and 20.

3.3.3. Voronoï tessellation type grains

The anisotropic structure derived from Voronoï tessellation with three principal axes (L), (LT) and (ST) and elongation along these axes is the same as in the previous section. Configurations after corrosion progress are shown in Fig. 22.

In Fig. 23, two perpendicular vertical sections into the material are shown. Again, the characteristic V-shaped groove is seen in CP and BP geometries and is also observed experimentally [57,17]. Here the reentrant V-shape can have a larger number of orientations according to the direction of the intergranular region. We also point out the merging of two corrosion fronts that will likely lead to a grain detachment or the formation of cavities (Fig. 23 top-right).

The linear regressions for height and angles of the equivalent systems, are respectively $h_r(t) = 4108 - 0.8107t$, $\theta = 35.8^\circ$ for the IVT, $h_r(t) = 4102 - 0.9369t$, $\theta = 20.5^\circ$ for corrosion parallel to the (L) direction, $h_r(t) = 4101 - 0.9269t$, $\theta = 22.0^\circ$ for corrosion parallel to the (LT) direction, $h_r(t) = 4096 - 0.5665t$, $\theta = 55.5^\circ$ for corrosion parallel to the (ST) direction. As in Section 3.2, the absolute value of the coefficient in front of t gives directly the effective corrosion rate

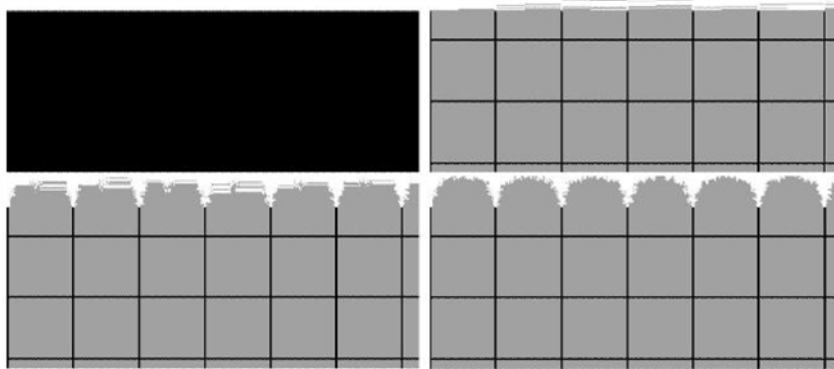


Fig. 17. Sections of the CP after detachment of the grains. The first two images are for the intergranular plane and the next plane. The following ones are for planes placed an eighth and across the middle of the elementary cube.

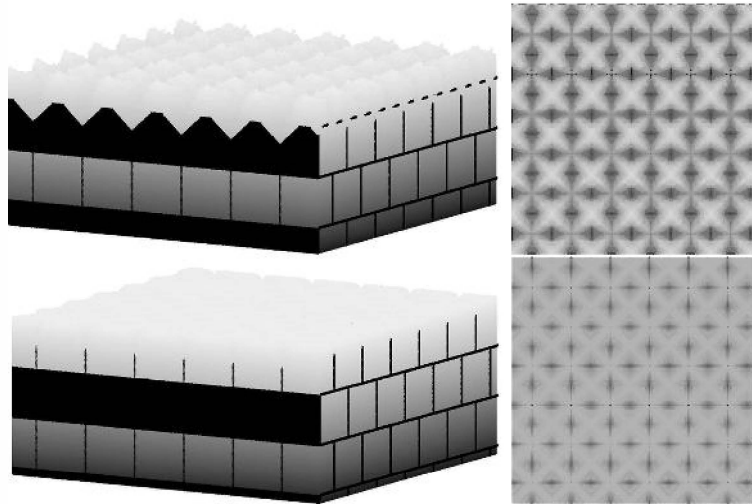


Fig. 18. Initial side and top views of the BP at two characteristic times before detachment and after detachment in presence of intragranular corrosion.

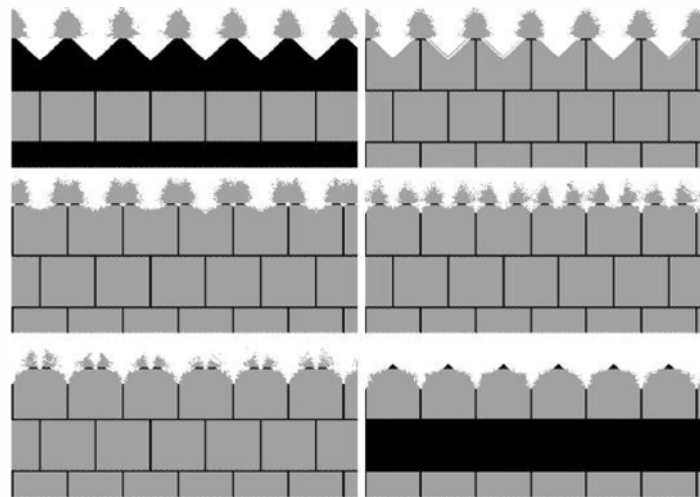


Fig. 19. Sections of the BP before detachment of the grains. To the exception of the first two images which show the intergranular plane and the next plane, all other planes are spaced of 8 planes, which corresponds to an eighth of the grain size. The planes beyond the 32nd plane are not shown as they are symmetric with respect to the middle of the elementary cube.

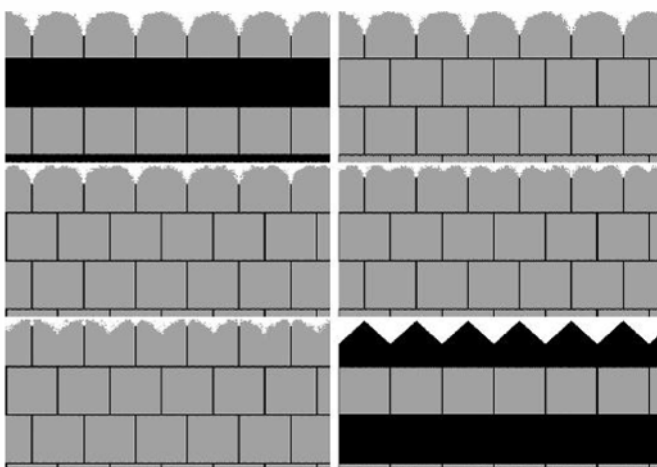


Fig. 20. Sections of the BP after detachment of the grains. To the exception of the first two images which show the intergranular plane and the next plane, all other planes are spaced of 8 planes, which corresponds to an eighth of the grain size.

in mm/y in our case where a corrosion rate of 1 mm/y and $p_{ig} = 1$ is assumed for the intergranular material. The results are practically identical to the case in absence of intergranular corrosion, indicating that the main mechanism of mass loss is the mechanism related to the intergranular corrosion. The only noticeable difference concerns the (ST) case where the intragranular corrosion in the smaller dimension of the grains can more efficiently help the detachment of grains. The different kinetics are similar to those found in the absence of intragranular corrosion. As for CP and BP, the corrosion remains dominated by the detachment of grains related to the intergranular region corrosion. The only noticeable difference relates to the grain plaquettes oriented parallel to the surface. There, the corrosion rate is slightly higher than in the absence of intragranular corrosion.

The roughness is shown in Fig. 24. Note that in all cases the roughness is much lower than in the absence of intragranular corrosion. The corrosion of the grains themselves levels out the surface. The effect is more pronounced for the (L) and (LT) directions, where plaquettes are perpendicular to the surface and show higher roughness values in the absence of intragranular corrosion. This leads to even smaller roughness than the IVT case. The

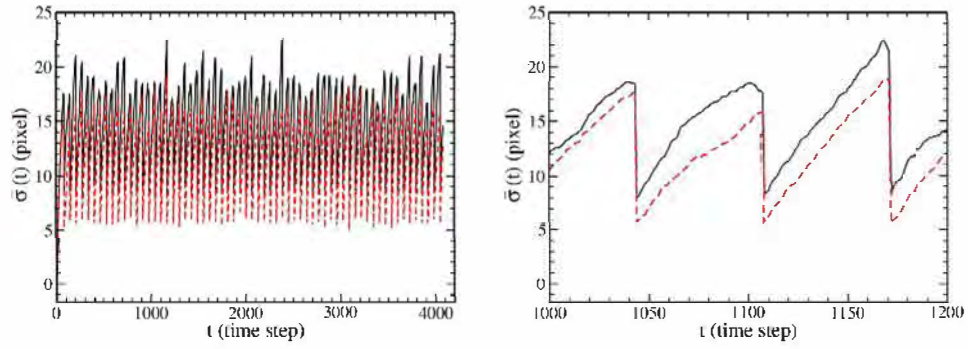


Fig. 21. Roughness for the CP and BP geometries identical colour code as in Fig. 2, detail of the curves on the right.

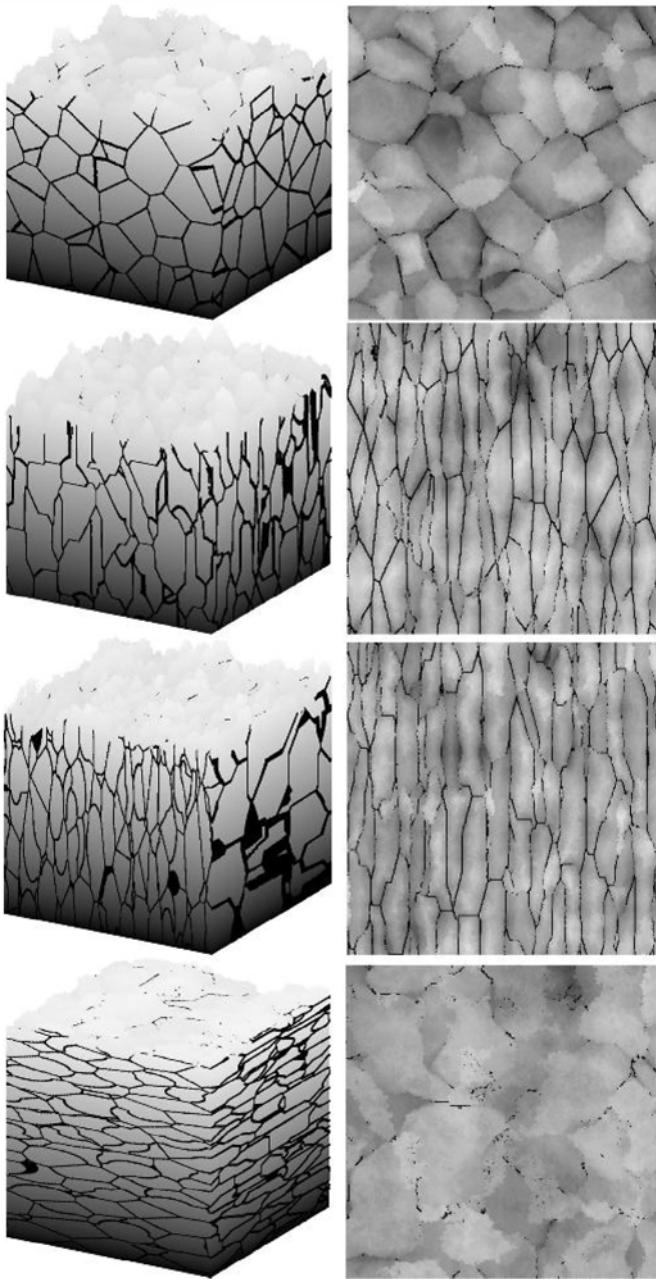


Fig. 22. Side and top views of the corroded system in the presence of intragranular corrosion for IVT and grains elongated as in Fig. 11.

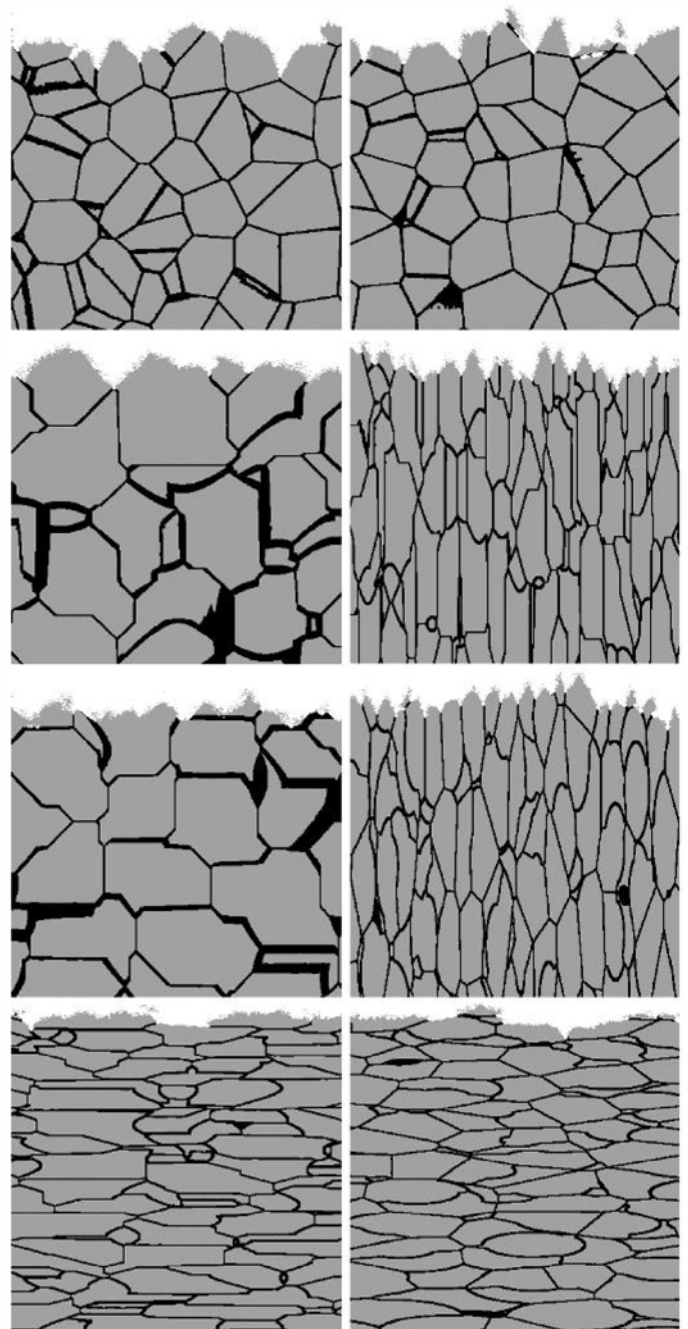


Fig. 23. Two perpendicular vertical sections of the metal for the systems of Fig. 22.

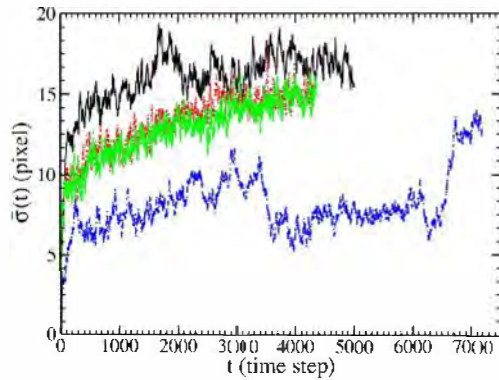


Fig. 24. Roughness as a function of time t for the geometries used in Fig. 9, with combined inter and intragranular corrosion. The same colour codes as in Fig. 10.

corrosion parallel to (ST) direction also leads to a smaller roughness as the largest surface of the plaquettes is parallel to the outer surface.

4. Conclusion

This paper presents a model investigating the effects of geometry on intergranular corrosion as well as the combined effects of inter and intragranular corrosion. The approach generalizes previous 2D models. Various grain geometries, isotropic or anisotropic, and different layouts are examined.

Sinuosity of the corrosion paths is found to play a similar role as in 2D. The effective corrosion rate is much smaller when the grain geometries and their layout force long deviations from the shortest corrosion path i.e. the straight line perpendicular to the metal surface. The susceptibility of grains to detachment depends upon the anisotropy of the grains. Moreover, the 3D extension of the model shows a larger variety of grain geometries as well as scenarios of grain detachment compared to simple extrapolation of 2D geometries. The predicted corrosion is, in general, faster than in the 2D case as shown in this paper.

When both inter and intragranular corrosion are present, the characteristic V-shaped grooves, found experimentally, are formed and their angle indicates the ratio of inter to intragranular corrosion rates. However, owing to faster intergranular corrosion, the overall corrosion rate remains generally fixed by the intergranular corrosion.

References

- [1] M.R. Stoudt, R.E. Ricker, The relationship between grain size and the surface roughening behavior of Al–Mg alloys, *Metall. Mater. Trans.* 33A (2002) 2283–2889.
- [2] R.B. Alvarez, H.J. Martin, M.F. Horstemeyer, M.Q. Chandler, N. Williams, P.T. Wang, A. Ruiz, Corrosion relationships as a function of time and surface roughness on a structural AE44 magnesium alloy, *Corros. Sci.* 52 (2010) 1635–1648.
- [3] K. Sasaki, G. Burstein, The generation of surface roughness during slurry erosion–corrosion and its effect on the pitting potential, *Corros. Sci.* 38 (1996) 2111.
- [4] J.R. Davis, Corrosion of aluminum and aluminum alloys, in: *ASM International Handbook Committee, ASM International, Materials Park, OH, 1999.*
- [5] P.R. Roberge, *Corrosion Inspection and Monitoring*, John Wiley & Sons, NY, 2007.
- [6] A. La Fontaine, H.-W. Yen, P. Trimby, S. Moody, S. Miller, M. Chensee, S. Ringer, J. Cairney, Martensitic transformation in an intergranular corrosion area of austenitic stainless steel during thermal cycling, *Corros. Sci.* 85 (2014) 1–6.
- [7] A. Stratulat, J.A. Duff, T.J. Marrow, Grain boundary structure and intergranular stress corrosion crack initiation in high temperature water of a thermally sensitised austenitic stainless steel, observed in situ, *Corros. Sci.* 85 (2014) 428–435.
- [8] M. Dhondt, I. Aubert, N. Saintier, J.M. Olive, Effects of microstructure and local mechanical fields on intergranular stress corrosion cracking of a friction stir welded aluminum–copper–lithium 2050 nugget, *Corros. Sci.* 86 (2014) 123–130.
- [9] A. Egbewande, W. Chen, R. Eadie, R. Kania, G.V. Boven, R. Worthingham, J. Been, Transgranular crack growth in the pipeline steels exposed to near-neutral pH soil aqueous solutions: discontinuous crack growth mechanism, *Corros. Sci.* 83 (2014) 343–354.
- [10] M.M. Sharma, J.D. Tomedi, J.M. Parks, A microscopic study on the corrosion fatigue of ultra-fine grained and conventional Al–Mg alloy, *Corros. Sci.* 93 (2015) 180–190.
- [11] X. Sun, B. Zhang, H. Lin, Y. Zhou, L. Sun, J. Wang, E.-H. Han, W. Ke, Correlations between stress corrosion susceptibility and grain boundary microstructures for an Al–Zn–Mg alloy, *Corros. Sci.* 77 (2013) 103–112.
- [12] D. Spencer, M. Edwards, M. Wenman, C. Tsitsios, G. Scatigno, P. Chard-Tuckey, The initiation and propagation of chloride-induced transgranular stress-corrosion cracking (TGSCC) of 304L austenitic stainless steel under atmospheric conditions, *Corros. Sci.* 88 (2014) 76–88.
- [13] Y. Zhou, Y. Zuo, The intergranular corrosion of mild steel in $\text{CO}_2 + \text{NaNO}_2$ solution, *Electrochim. Acta* 154 (2015) 157–165.
- [14] S. Tachibana, Y. Kuronuma, T. Yokota, K. Yamada, Y. Moriya, C. Kami, Effect of hot rolling and cooling conditions on intergranular corrosion behavior in alloy625 clad steel, *Corros. Sci.* 99 (2015) 125–133.
- [15] H. Li, P. Zhao, Z. Wang, Q. Mao, B. Fang, R. Song, Z. Zheng, The intergranular corrosion susceptibility of a heavily overaged Al–Mg–Si–Cu alloy, *Corros. Sci.* 107 (2016) 113–122.
- [16] J. Li, N. Birbilis, D. Liu, Y. Chen, X. Zhang, C. Cai, Intergranular corrosion of Zn-free and Zn-microalloyed Al–xCu–yLi alloys, *Corros. Sci.* 105 (2016) 44–57.
- [17] B. Gwinner, M. Auroy, F. Balbaud-C  lerier, P. Fauvet, N. Larabi-Gruet, P. Laghoutaris, R. Robin, Towards a reliable determination of the intergranular corrosion rate of austenitic stainless steel in oxidizing media, *Corros. Sci.* 107 (2016) 60–75.
- [18] F. Shi, P. Tian, N. Jia, Z. Ye, Y. Qi, C. Liu, X. Li, Improving intergranular corrosion resistance in a nickel-free and manganese-bearing high-nitrogen austenitic stainless steel through grain boundary character distribution optimization, *Corros. Sci.* 107 (2016) 49–59.
- [19] P. Meakin, T. J  ssang, J. Feder, Simple passivation and depassivation model for pitting corrosion, *Phys. Rev. E* 48 (4) (1993) 2906–2916.
- [20] L. Bal  zs, J.F. Gouyet, Two-dimensional pitting corrosion of aluminium thin layers, *Physica A* 217 (3–4) (1995) 319–338.
- [21] L. Li, X. Li, C. Dong, Y. Huang, Computational simulation of metastable pitting of stainless steel, *Electrochim. Acta* 54 (26) (2009) 6389–6395.
- [22] D. di Caprio, C. Vautrin-Ul, J. Stafiej, J. Saunier, A. Chauss  , D. F  ron, J.P. Badiali, Morphology of corroded surfaces: contribution of cellular automaton modelling, *Corros. Sci.* 53 (1) (2011) 418–425.
- [23] D. di Caprio, J. Stafiej, Simulations of passivation phenomena based on discrete lattice gas automata, *Electrochim. Acta* 55 (12) (2010) 3884–3890.
- [24] D. di Caprio, J. Stafiej, The role of adsorption in passivation phenomena modelled by discrete lattice gas automata, *Electrochim. Acta* 56 (11) (2011) 3963–3968.
- [25]  . Bartosik, D. di Caprio, J. Stafiej, Cellular automata approach to corrosion and passivity phenomena, *Pure Appl. Chem.* 85 (1) (2012) 247–256.
- [26] K.-C. Lan, Y. Chen, T.-C. Hung, H.-M. Tung, G.-P. Yu, Simulation of the growth of oxide layer of stainless steels with chromium using cellular automaton model: verification and parameter study, *Comput. Mater. Sci.* 77 (2013) 139–144.
- [27] H. Wang, E.-H. Han, Simulation of metastable corrosion pit development under mechanical stress, *Electrochim. Acta* 90 (2013) 128–134.
- [28] P. Van der Wee n, A.M. Zimer, E.C. Pereira, L.H. Mascaro, O.M. Bruno, B. De Baets, Modeling pitting corrosion by means of a 3D discrete stochastic model, *Corros. Sci.* 82 (2014) 133–144.
- [29] C.F. P  rez-Brokate, D. di Caprio, D. F  ron, J. De Lamare, A. Chauss  , Overview of cellular automaton models for corrosion, *Lect. Notes Comput. Sci.* 8751 (2014) 187–196.
- [30] H. Wang, E.-H. Han, Computational simulation of corrosion pit interactions under mechanochemical effects using a cellular automaton/finite element model, *Corros. Sci.* 103 (2016) 305–311.
- [31] C.F. P  rez-Brokate, D. di Caprio, D. F  ron, J. de Lamare, A. Chauss  , Three dimensional discrete stochastic model of occluded corrosion cell, *Corros. Sci.* (2016), <http://dx.doi.org/10.1016/j.corsci.2016.04.009>.
- [32] A. Taleb, J. Stafiej, Numerical simulation of the effect of grain size on corrosion processes: surface roughness oscillation and cluster detachment, *Corros. Sci.* 53 (2011) 2508–2513.
- [33] S. Lishchuk, R. Akid, K. Worden, J. Michalski, A cellular automaton model for predicting intergranular corrosion, *Corros. Sci.* 53 (8) (2011) 2518–2526.
- [34] T. Igarashi, A. Komatsu, T. Motooka, F. Ueno, Y. Kaji, M. Yamamoto, Simulations of intergranular corrosion feature for stainless steel using cellular automata method, *Zairyo to Kankyo (Corros. Eng. Jpn.)* 63 (7) (2014) 431–437.
- [35] F. Ueno, A. Komatsu, T. Igarashi, M. Yamamoto, Study on the effect of phosphorous concentration on intergranular corrosion of stainless steel in boiling nitric acid solution, in: *Eurocorr, Pisa (Italy), 2014.*
- [36] T. Igarashi, A. Komatsu, T. Motooka, F. Ueno, M. Yamamoto, Three dimensional computational modelling and simulation of intergranular corrosion propagation of stainless steel, in: *19th International Corrosion Congress, Jeju, Korea, 2014, pp. 1–7.*
- [37] M. Gu  rin, J. Alexis, E. Andrieu, L. Laffont, W. Lefebvre, G. Odemer, C. Blanc, Identification of the metallurgical parameters explaining the corrosion

- susceptibility in a 2050 aluminium alloy, *Corros. Sci.* 102 (2016) 291–300.
- [38] C. Vautrin-UI, A. Taleb, J. Stafiej, A. Chaussé, J. Badiali, Mesoscopic modelling of corrosion phenomena: coupling between electrochemical and mechanical processes, analysis of the deviation from the faraday law, *Electrochim. Acta* 52 (2007) 5368–5376.
- [39] H. Grabke, Grain boundary segregation of impurities in iron and steels and effects on steel properties, in: C. Briant (Ed.), *Impurities in Engineering Materials*, Marcel Dekker Inc., New York, 1999, pp. 143–192.
- [40] C. Briant, The effect of grain boundary segregation on intergranular failures, in: C. Briant (Ed.), *Impurities in Engineering Materials*, Marcel Dekker Inc., New York, 1999, pp. 193–224.
- [41] C. Vargel, Chapter B.2 – types of corrosion on aluminium, in: C. Vargel (Ed.), *Corrosion of Aluminium*, Elsevier, Amsterdam, 2004, pp. 113–146.
- [42] J.K. Kim, Y.H. Kim, J.S. Lee, K.Y. Kim, Effect of chromium content on intergranular corrosion and precipitation of Ti-stabilized ferritic stainless steels, *Corros. Sci.* 52 (5) (2010) 1847–1852.
- [43] S.-X. Li, Y.-N. He, S.-R. Yu, P.-Y. Zhang, Evaluation of the effect of grain size on chromium carbide precipitation and intergranular corrosion of 316L stainless steel, *Corros. Sci.* 66 (2013) 211–216.
- [44] B.S. Kumar, B.S. Prasad, V. Kain, J. Reddy, Methods for making alloy 600 resistant to sensitization and intergranular corrosion, *Corros. Sci.* 70 (2013) 55–61.
- [45] P. Lejček, *Grain Boundary Segregation in Metals Springer Series in Materials Science*, vol. 136, 1st edition, Springer-Verlag Berlin Heidelberg, 2010.
- [46] H.-J. Kim, S.-H. Jeon, S.-T. Kim, I.-S. Lee, Y.-S. Park, K.-T. Kim, Y.-S. Kim, Investigation of the sensitization and intergranular corrosion of tube-to-tubesheet welds of hyper duplex stainless steel using an electrochemical reactivation method, *Corros. Sci.* 87 (2014) 60–70.
- [47] S.-H. Jeon, D.H. Hur, H.-J. Kim, Y.-S. Park, Effect of Ce addition on the precipitation of deleterious phases and the associated intergranular corrosion resistance of 27Cr–7Ni hyper duplex stainless steels, *Corros. Sci.* 90 (2015) 313–322.
- [48] P.-J. Cunat, *Aciers inoxydables critères de choix et structure, Techniques de l'ingénieur: Aciers inoxydables, aciers réfractaires et aciers résistant au fluage M4540* (2000) 1–17.
- [49] M.P. Seah, Grain boundary segregation, *J. Phys. F: Met. Phys.* 10 (6) (1980) 1043.
- [50] F. Christien, R.L. Gall, G. Saindrenan, Phosphorus grain boundary segregation in steel 17-4 PH, *Scr. Mater.* 48 (1) (2003), 11–16, 301–306.
- [51] M. Lucas, J. Stafiej, C. Slim, S. Delpech, D. di Caprio, Cellular automata modeling of scanning electrochemical microscopy (SECM) experiments, *Electrochim. Acta* 145 (2014) 314–318.
- [52] C.F. Pérez-Brokate, D. di Caprio, E. Mahé, D. Féron, J. de Lamare, Cyclic voltammetry simulations with cellular automata, *J. Comput. Sci.* 11 (2015) 269–278.
- [53] S.H. Whang (Ed.), *Nanostructured Metals and Alloys, Woodhead Publishing Series in Metals and Surface Engineering*, Woodhead Publishing, 2011.
- [54] W. Tian, S. Li, X. Chen, J. Liu, M. Yu, Intergranular corrosion of spark plasma sintering assembled bimodal grain sized AA7075 aluminum alloys, *Corros. Sci.* 107 (2016) 211–224.
- [55] Y. Goueffon, L. Arurault, C. Mabru, C. Tonon, P. Guigue, Black anodic coatings for space applications: study of the process parameters, characteristics and mechanical properties, *J. Mater. Process. Technol.* 209 (2009) 5145–5151.
- [56] L. Beaunier, M. Froment, C. Vignaud, A kinetical model for the electrochemical grooving of grain boundaries, *Electrochim. Acta* 25 (10) (1980) 1239–1246.
- [57] V. Bague, S. Chachoua, Q.T. Tran, P. Fauvet, Determination of the long-term intergranular corrosion rate of stainless steel in concentrated nitric acid, *J. Nucl. Mater.* 392 (2009) 396–404.